Chemical Engineering Science 106 (2014) 198–210

Contents lists available at ScienceDirect

Chemical Engineering Science

journal homepage: www.elsevier.com/locate/ces

Three-dimensional tool design for steady-state electrochemical machining by continuous adjoint-based shape optimization

Jinming Lu [a,*], Gerwin Riedl [a], Bernhard Kiniger [b], Ewald A. Werner [a]

[a] Lehrstuhl für Werkstoffkunde und Werkstoffmechanik, Technische Universität München, Boltzmannstraße 15, 85748 Garching, Germany
[b] Lehrstuhl für Optimale Steuerung, Technische Universität München, Boltzmannstraße 3, 85748 Garching, Germany

HIGHLIGHTS

- We propose a method to solve the tool design problem in electrochemical machining in two and three dimensions.
- We use continuous adjoint-based shape optimization combined with elements of shape calculus.
- A comparison with exact analytic solution demonstrates the accuracy of the method.
- We investigate the influence of electrode curvature on the front gap width.
- The inaccuracies of the cos θ-method for curved electrodes can be estimated.

ARTICLE INFO

Article history:
Received 28 July 2013
Received in revised form
19 October 2013
Accepted 20 November 2013
Available online 2 December 2013

Keywords:
Design
Electrochemistry
Materials processing
Numerical analysis
Optimization

ABSTRACT

In electrochemical machining (ECM), it is important to design the shape of an appropriate tool capable of producing a workpiece of desired shape. This work presents a numerical approach to solving the two- and three-dimensional tool design problem in steady-state ECM. The tool design problem is transformed into a shape optimization problem and then solved using the continuous adjoint method combined with elements of shape calculus, ensuring high efficiency and the maximum possible degrees of freedom. A numerical experiment on a two-dimensional Gaussian-shaped workpiece shows a good agreement of the calculated tool shape with the exact analytical solution. Tool design is carried out for a series of two- and three-dimensional workpiece shapes to investigate the influence of the curvature of the desired workpiece on the front gap width in steady-state ECM.

1. Introduction

Electrochemical machining (ECM) is a non-conventional materials processing technique used to produce parts of complex shapes made of high-strength alloys, irrespective of their hardness and without introducing residual stress. For the last five decades, ECM-related techniques have been developed intensively. Already to the end of 1974, more than 1200 related scientific articles were published (Bannard, 1977); several review articles (Bannard, 1977; Rajurkar et al., 1999) and monographs (De Barr and Oliver, 1968; Faust, 1971; McGeough, 1974) provide an overview of the topic. Today, applications of ECM range from the production of turbine disks and blades for aerospace industry (e.g. Lamphere et al., 2007) to shaping three-dimensional (3D) structures with submicrometer precision (e.g. Schuster et al., 2000).

In an ECM process depicted schematically in Fig. 1(a), a metallic tool of defined shape is advanced towards a metallic workpiece at a specified tool feed rate (velocity). The interelectrode gap is filled with appropriate electrolyte (e.g. NaCl, $NaNO_3$). An external DC voltage is applied such that the negatively polarized tool is the cathode, and the positively polarized workpiece is the anode of an electrolytic cell.[1] Electric current flows across the interelectrode gap due to electrochemical reactions at the surfaces of both electrodes. While the tool shape is not changed since hydrogen or nitrate (Mao, 1971) reduction usually takes place at its surface, metal atoms at the workpiece are oxidized to ions. These ions dissolve into the electrolyte which is pumped through the interelectrode gap to prevent boiling by Ohmic heating and to sweep away the reaction products. Due to the current density distribution at its surface, the shape of the workpiece approaches the negative image of the tool, as schematically shown in Fig. 1(b).

* Corresponding author. Tel.: +49 8928915312.
E-mail address: Lu@wkm.mw.tum.de (J. Lu).

[1] In this work, the expressions tool/cathode and workpiece/anode are used as "synonym pairs", respectively.

0009-2509/$ - see front matter © 2013 Elsevier Ltd. All rights reserved.
http://dx.doi.org/10.1016/j.ces.2013.11.040

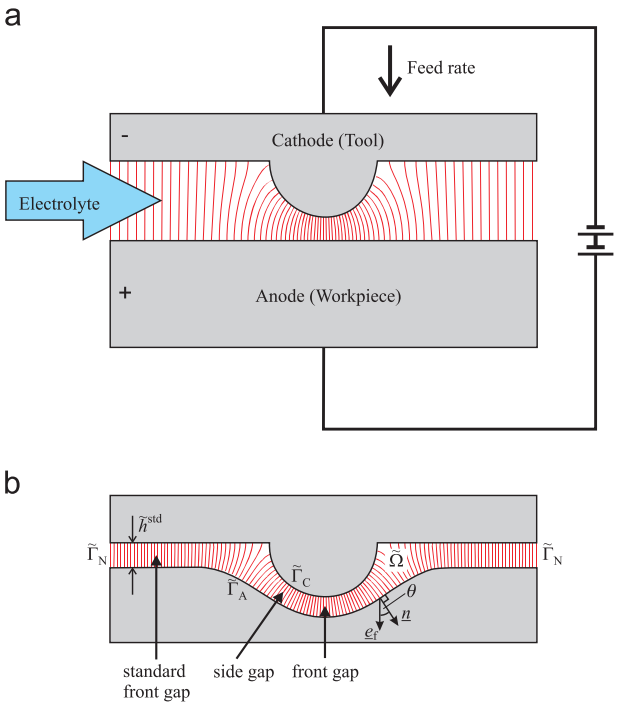

Fig. 1. Basic principle of electrochemical machining (ECM). Panel (a) shows the initial machining configuration consisting of a cathode tool of a defined shape and a plane anode workpiece to be machined. The tool is advanced towards the workpiece at a defined feed rate. Electric current flows when a voltage is applied across the gap; the thin red lines between the electrodes illustrate the current density. Panel (b) shows the steady state configuration of tool and workpiece. The final shape of the workpiece is approximately the negative image of the tool electrode. The inter-electrode gap is the calculation domain $\tilde{\Omega}$ of the model used in this work. The boundaries $\tilde{\Gamma}_C$ and $\tilde{\Gamma}_A$ are defined by tool (cathode) and workpiece (anode) surfaces, respectively, and $\tilde{\Gamma}_N$ is the side boundary through which the electric current flux is zero. For each point on the workpiece boundary $\tilde{\Gamma}_A$, θ is defined as the angle between the outer boundary unit normal vector $\underline{n}$ and the feed direction unit vector $\underline{e}_f$. "Front gap" refers to an inter-electrode gap region where the workpiece surface is perpendicular to the feed direction (i.e. $\theta = 0$). "Standard front gap" with width $\tilde{h}^{std}$ is a front gap region where the electrodes are plane. All other regions of the inter-electrode gap are called "side gap". (For interpretation of the references to color in this figure caption, the reader is referred to the web version of this article.)

Apart from understanding the physical phenomena related to high-rate metal dissolution (e.g. Datta, 1993) and realizing reliable process control, a further problem associated with ECM concerns accurately relating the shape of the workpiece to that of the tool. The *direct problem* in ECM refers to predicting the workpiece shape evolution for a given tool shape, whereas the *inverse problem* deals with designing the shape of the tool capable of producing a desired workpiece shape under specified machining conditions.

The direct problem in ECM is related to the cathode shape change problem in electrodeposition; both have been studied using analytical and numerical techniques. Fitz-Gerald and McGeough (1969) expanded two-dimensional (2D) electrode shapes into Fourier series to analyze surface smoothing during ECM analytically. Many numerical simulations were based on the so-called potential model, where the primary current distribution (definition cf. Ibl, 1981) is taken into account. Alkire et al. (1978) employed the finite element method (FEM) to predict the cathode shape change in electrodeposition. Sautebin et al. (1980) used FEM to calculate workpiece surface smoothening in ECM. Białecki et al. (1984) and Deconinck (1994) used the boundary element method (BEM) to calculate primary current distribution in ECM. Concepts of 3D ECM computer simulations were proposed by Davydov et al. (2004); practical 3D ECM simulations based on the primary current distribution were implemented in commercial software packages (e.g. Purcar et al., 2004).

Beyond the potential model, Prentice and Tobias (1982) calculated changing electrode profiles in electrodeposition, taking electrode kinetics into account by boundary conditions based on the Butler–Volmer equation. Hourng and Chang (1993) and Kozak (1998) developed mathematical models for ECM-related process simulations accounting for the influence of Ohmic heating and gas fraction on the conductivity. Electrolyte flow in a 3D ECM model was considered by Fujisawa et al. (2008). Recently, complex ECM simulations involving multi-ion transport were presented (Deconinck et al., 2012a).

The inverse tool design problem, which is the topic of this work, is more important for industrial applications. To our knowledge, main non-experimental approaches to this problem encompass approximative analytical, exact analytical, iterative numerical, and non-iterative numerical methods.

The so-called $\cos\theta$—method is an approximative analytical method employed by Tipton (1971), assuming the gap width to be inversely proportional to $\cos\theta$, where θ is the angle between the tool feed direction and the normal of the workpiece boundary (cf. Fig. 1(b)). According to De Barr and Oliver (1968), this method is applicable for $\theta < 60°$. But even for the front gap ($\theta = 0$), the $\cos\theta$—method will only yield results with inaccuracies of less than 10% if the radius of curvature of the workpiece surface is at least one order of magnitude larger than the gap width, as will be shown in Section 4.

The exact analytical method for 2D tool design problems proposed by Krylov (1968), Nilson and Tsuei (1974) relies on the harmonic property of real- and imaginary parts of holomorphic functions and the principle of analytic continuation. For workpiece shapes that are representable by $y = F(x)$ with an analytic function F, the shapes of the tool can be obtained as parametric curves in 2D. Alder et al. (2000) combined this method with Fourier series to represent more general 2D workpiece shapes. For another exact approach proposed by Lacey (1985), a harmonic function Ψ has to be determined in a way that its gradient describes the position vector field of the workpiece surface. The method is exemplarily applied to a special 3D problem, but calculation of Ψ for general workpiece shapes is difficult.

A numerical approach to the ECM tool design problem without tool movement is reformulating it as an elliptic variational inequality (Elliott, 1980). Butt (1993) presented applications of this method to the dissolution of a workpiece that is fully surrounded by the tool. Liu and Rubio (1991) proved the existence of the solution mathematically. Although the industrially more relevant case with moving tool electrode was not presented, the method could be used for tool design in non-steady-state ECM (Butt, 1993).

Starting from an initial guess of the tool shape, some researchers correct the tool iteratively based on numerical solutions of the direct problem to overcome the ill-posedness of the inverse problem. Reddy et al. (1988) developed a correction factor method that adjusts the tool shape based on the calculated anode profile to an assumed tool. Narayanan et al. (1986) and Hardisty and Mileham (1999) converted the deviation of the current density on a workpiece point from the desired value into a positional error of the tool point along the same current flux line, which is then used to correct the tool. Hunt (1990) employed an embedding method that searches among the solutions of the direct problem.

Iterative numerical tool design methods can also be based on optimization. Das and Mitra (1992) used BEM, Zhou and Derby (1995) used FEM to calculate the electric potential and defined the sum of squared difference between actual and required current density at all node points at the workpiece boundary as the objective function to be minimized. The tool is represented by Fourier series with coefficients as design variables. In the optimization procedure, partial derivatives of the objective function with

respect to the design variables are calculated using finite difference approximations. A similar approach based on optimization with Fourier coefficients as design variables was used by Chang and Hourng (2001) who additionally incorporated the effects of thermal-fluid properties of the electrolyte.

A non-iterative numerical method was developed by McClennan et al. (2006) for 2D tool design based on the solution of a set of ordinary differential equations. Zhu et al. (2003) pioneered in a non-iterative numerical tool design method by successive application of both boundary conditions (cf. Eqs. (15) and (16)) on the workpiece boundary to calculate the electric potential distribution; the tool shape is then determined as an equipotential curve. This method was extended to 3D tool design problems (Sun et al., 2006). However, the method requires structured computational meshes, and since the successive application of both conditions on the same boundary requires a non-standard numerical scheme compared to the solution of conventional boundary value problems, much effort is required to develop the simulation environment.

In this work, we present the derivation, implementation and some basic examples of steady-state ECM tool design by adjoint-based shape optimization using shape derivatives. The aim is to develop a concept for a flexible, simple to implement and efficient method for the tool design procedure in ECM. Our work is based on some existing concepts to a certain extent:

1. Our method shares the concept of iterative optimization with the methods proposed by Das and Mitra (1992), Zhou and Derby (1995), or Chang and Hourng (2001); however, we do not parametrize the tool shape as a sum of predefined basis functions and we use a more efficient way to calculate the gradient.
2. Our method operates directly on a computational mesh like the method proposed by Zhu et al. (2003) or Sun et al. (2006), but it does not require special implementation of numerical schemes to solve the Laplace equation layer by layer.

The latter concept, working directly on a computational mesh, ensures the maximum flexibility; however, it is associated with many design variables which are the positions of the moving boundary points. In this case, the finite difference-based calculation of the gradient of the objective function with respect to the design variables is rather time consuming. In this work, the problem of handling many design variables is solved using two important ingredients:

1. The *adjoint-method*, also known as the *control theory approach* (Lions, 1968) to solve equality-constrained optimization problems, calculates the gradient of the objective function via the solution of an adjoint equation for a Lagrange multiplier; the adjoint equation is solved once per iteration in the optimization procedure, independent of the number of design variables.
2. The so-called *shape derivatives* as a basic element of *shape calculus* (e.g. Sokołowski and Zolésio, 1992) enable the study of changes in the objective function(al) of a shape optimization problem with respect to shape variations of the object of interest.

The so-called adjoint-based shape optimization method, which is already successfully applied in e.g. airfoil design, uses the control theory approach of calculating gradients (ingredient 1 from above) in cases where the design variables are related to the shape of an object of interest. To incorporate geometrical information into optimization, the shape to be optimized can be parametrized as a function of design variables (e.g. Jameson and Martinelli, 2000); the shape variation is carried out by a coordinate transformation. Instead of geometry parametrization, Schmidt et al. (2011) presented an alternative approach using elements of shape calculus (ingredient 2 from above), preserving the shape optimization nature of the problem. This approach has the advantage of circumventing the costly calculation of the "mesh sensitivity Jacobian" which would be necessary if the shape to be optimized were parametrized by a function of a finite dimensional design variable vector (Gauger et al., 2012).

For solving the tool design problem in ECM, we use the adjoint-based shape optimization method using shape derivatives, which is presented by Schmidt et al. (2011). The adjoint equation is derived in a continuous form and discretized afterwards. For the discretization, we use the finite volume method (FVM) to solve the governing equations since FVM is locally conservative by design and thus suitable for the potential equation derived from charge conservation. The solver is implemented using a freely available, open source software package.

After a short introduction of the theoretical basis of this work (cf. Section 2), which includes the potential model and constrained optimization, the tool design procedure is derived in detail in Sections 3, Appendix A and B, using adjoint-based optimization combined with elements of shape calculus. After the description of the implementation of the solver (cf. Section 3.2.1), the method is exemplarily applied to tool design for curved 2D and 3D workpiece geometries in Section 4.

2. Theoretical background

2.1. The potential model of ECM

The complexity of ECM process models largely depends on the physical and chemical phenomena taken into account when calculating the current density in the inter-electrode gap. Although more sophisticated ECM process simulation models (e.g. Deconinck et al., 2012b) exist, we use the simplified potential model to describe the current density in this work, since we mainly focus on the use of adjoint-based shape optimization combined with shape derivatives to solve the tool design problem in ECM rather than on the influence of process conditions on the machining result. In the simplified potential model, five assumptions are made, namely (cf. Zhou and Derby, 1995):

1. The electrolyte flow rate is assumed to be high enough to provide effective flushing, resulting in a homogeneous conductivity distribution within the inter-electrode gap.
2. The current flow across the gap is solely due to anodic metal dissolution at constant valency, giving rise to a constant current efficiency.
3. The kinetics of the electrode reactions are sufficiently fast that overpotential effects are negligible.
4. The workpiece shape change due to metal dissolution occurs in the direction of the surface normal.
5. The tool feed rate and the machining voltage take constant positive values throughout the whole process.

These assumptions lead to a mathematical model for ECM governed by the following equations (a tilde ˜ indicates a dimensioned quantity in this work):

1. The electric potential $\tilde{\Phi}$ (in V) obeys the Laplace equation

$$\underline{\tilde{\nabla}} \cdot (\tilde{\kappa} \underline{\tilde{\nabla}} \tilde{\Phi}) = 0 \quad \text{in } \tilde{\Omega} \tag{1}$$

$$\frac{\partial\tilde{\Phi}}{\partial\tilde{n}}=0 \quad \text{on } \tilde{\Gamma}_N \tag{2}$$

$$\tilde{\Phi}=0 \quad \text{on } \tilde{\Gamma}_C \tag{3}$$

$$\tilde{\Phi}=\tilde{U} \quad \text{on } \tilde{\Gamma}_A \tag{4}$$

with electrolyte conductivity $\tilde{\kappa}$ (in $(\Omega m)^{-1}$) and machining voltage $\tilde{U}$ (in V); $\tilde{\Omega}$ denotes the calculation domain (i.e. the inter-electrode gap, cf. Fig. 1(b)), $\tilde{\Gamma}_N$ the non-metallic side boundaries, $\tilde{\Gamma}_C$ the tool (cathode) surface, and $\tilde{\Gamma}_A$ the workpiece (anode) surface.

2. The current density $\underline{\tilde{j}}$ is given by Ohm's law

$$\underline{\tilde{j}}=-\tilde{\kappa}\underline{\tilde{\nabla}}\tilde{\Phi} \quad \text{in } \tilde{\Omega}. \tag{5}$$

3. The volume dissolution rate $\dot{\tilde{V}}$ at the anode is controlled by Faraday's law

$$\dot{\tilde{V}}=\frac{\tilde{M}}{\tilde{\rho}z\tilde{F}}\tilde{I}, \tag{6}$$

where $\tilde{M}$ is the molar mass, $\tilde{\rho}$ is the density of the anode (workpiece) metal, z is the valency of the anode metal, $\tilde{F}$ is the Faraday constant, and $\tilde{I}$ is the total current. Hence, a surface point of the workpiece boundary $\tilde{\Gamma}_A$ moves at the velocity (cf. Deconinck, 1994)

$$\underline{\tilde{v}}_A=\frac{\tilde{M}}{\tilde{\rho}z\tilde{F}}|\underline{\tilde{j}}_A|\underline{n}=\tilde{\kappa}\tilde{K}_V\left.\frac{\partial\tilde{\Phi}}{\partial\tilde{n}}\right|_{\tilde{\Gamma}_A}\underline{n} \tag{7}$$

due to dissolution, where $\underline{\tilde{j}}_A$ denotes the current density and $\underline{n}$ is the outer unit normal of the workpiece boundary at this surface point; the constant $\tilde{K}_V=\tilde{M}/(\tilde{\rho}z\tilde{F})$ has the meaning of the dissolved volume per unit charge, which depends on the metallic material being machined.

2.2. Steady-state condition and the tool design problem

The evolution of the standard front gap width $\tilde{h}^{std}$ (cf. Fig. 1(b)) is obtained by applying the potential model to an ECM process using plane parallel tool and workpiece electrodes which are perpendicular to the feed direction. With the uniform current density $|\underline{\tilde{j}}_A|=\tilde{\kappa}\tilde{U}/\tilde{h}^{std}$, the time derivative of the standard front gap width is given as

$$\frac{d\tilde{h}^{std}}{d\tilde{t}}=|\underline{\tilde{v}}_A|-\tilde{v}_f=\tilde{\kappa}\tilde{K}_V\left.\frac{\partial\tilde{\Phi}}{\partial\tilde{n}}\right|_{\tilde{\Gamma}_A}-\tilde{v}_f=\frac{\tilde{\kappa}\tilde{K}_V\tilde{U}}{\tilde{h}^{std}}-\tilde{v}_f, \tag{8}$$

where $\tilde{v}_f$ is the feed rate. The implicit solution of Eq. (8) is given by (Ch. 5 McGeough, 1974)

$$\tilde{t}=\frac{1}{\tilde{v}_f}\left[\tilde{h}^{std}(0)-\tilde{h}^{std}(\tilde{t})+\tilde{h}_e^{std}\ln\left(\frac{\tilde{h}(0)-\tilde{h}_e^{std}}{\tilde{h}(\tilde{t})-\tilde{h}_e^{std}}\right)\right] \tag{9}$$

where

$$\tilde{h}_e^{std}=\frac{\tilde{\kappa}\tilde{K}_V\tilde{U}}{\tilde{v}_f} \tag{10}$$

is the standard equilibrium front gap width obtained as the steady-state solution to Eq. (8) for $d\tilde{h}^{std}/d\tilde{t}=0$. As discussed by McGeough (1974), the gap width $\tilde{h}^{std}(\tilde{t})$ during a machining process starting with $\tilde{h}^{std}(0)\neq\tilde{h}_e^{std}$ will approach the equilibrium value where the material dissolution velocity is exactly compensated by the feed rate.

In ECM using non-planar electrodes, such a steady state also exists; it is characterized by the inter-electrode gap moving at the feed rate without changing its shape (Nilson and Tsuei, 1974). Thus, the normal component of the velocity of the workpiece boundary $\tilde{\Gamma}_A$ in a coordinate system tied to the tool boundary $\tilde{\Gamma}_C$ must vanish, i.e.

$$(\underline{\tilde{v}}_A-\tilde{v}_f\underline{e}_f)\cdot\underline{n}=\tilde{\kappa}\tilde{K}_V\left.\frac{\partial\tilde{\Phi}}{\partial\tilde{n}}\right|_{\tilde{\Gamma}_A}-\tilde{v}_f\cos\theta=0, \tag{11}$$

where $\underline{e}_f$ is the unit vector in feed direction (usually pointing to the negative z-direction of the coordinate system), and θ is the angle between the outer unit normal of the workpiece boundary and the feed direction (cf. Fig. 1(b)). For tool design in steady state machining, the following (inverse) problem has to be solved:

$$\underline{\tilde{\nabla}}\cdot(\tilde{\kappa}\underline{\tilde{\nabla}}\tilde{\Phi})=0 \quad \text{in } \tilde{\Omega} \tag{12}$$

$$\frac{\partial\tilde{\Phi}}{\partial\tilde{n}}=0 \quad \text{on } \tilde{\Gamma}_N \tag{13}$$

$$\tilde{\Phi}=0 \quad \text{on } \tilde{\Gamma}_C \text{ (unknown)} \tag{14}$$

$$\tilde{\Phi}-\tilde{U}=0 \quad \text{on } \tilde{\Gamma}_A \tag{15}$$

$$\frac{\tilde{\kappa}\tilde{K}_V}{\tilde{v}_f}\frac{\partial\tilde{\Phi}}{\partial\tilde{n}}-\cos\theta=0 \quad \text{on } \tilde{\Gamma}_A, \tag{16}$$

i.e. the shape of the tool boundary $\tilde{\Gamma}_C$ has to be determined in a way that the additional boundary condition given by Eq. (16) is satisfied.

2.3. Constrained optimization problems

Before transforming the steady-state ECM tool design problem given by Eqs. (12)–(16) into a constrained optimization problem, which is carried out in Section 3, we give a short sketch of the adjoint method used in this work, following the derivation proposed by Céa (1986). This method can be used to solve optimization problems with equality constraints, which are formulated as follows:

Find the design variable (vector) $\underline{a}$ such that

$$j(\underline{a})=J(\underline{a},\underline{s}(\underline{a}))\rightarrow\text{Min} \tag{17}$$

subject to

$$\underline{R}(\underline{a},\underline{s})=\underline{0}. \tag{18}$$

In Eq. (17), J is the objective function depending on both $\underline{a}$ and the state variable (vector) $\underline{s}$ that again depends on the design variable; j is the reduced objective function that only depends on the design variable $\underline{a}$ in total. In Eq. (18), $\underline{R}$ is a vector-valued function whose zero level-sets implicitly defines the equality constraints relating the design and the state variables; these constraints can represent e.g. system equations.

The optimization problem is solved using the reduced gradient approach originally proposed by Frank and Wolfe (1956). The idea is to transform the constrained optimization problem into an unconstrained one and then use e.g. the steepest descent method to find a minimum. The key step of this method is the calculation of the reduced gradient

$$D_a j=\partial_a J+\partial_s J\cdot D_a\underline{s}, \tag{19}$$

which is the gradient of the reduced objective function j with respect to the design variable. Knowing the value of $D_a j$ at a specific value $\underline{a}_0$ of the design variable, the directional derivative of j at $\underline{a}_0$ in a (search) direction $\underline{v}$ can then be calculated, namely

$$D_a j(\underline{a}_0)[\underline{v}]=\lim_{\varepsilon\rightarrow 0}\frac{j(\underline{a}_0+\varepsilon\underline{v})-j(\underline{a}_0)}{\varepsilon}=D_a j(\underline{a}_0)\cdot\underline{v}. \tag{20}$$

Hence, the function j decreases the fastest if the optimal search direction $\underline{v}^{opt}$ is chosen to be in the direction of the negative

gradient, i.e.

$$\underline{v}^{\mathrm{opt}} \parallel -\mathrm{D}_a j(\underline{a}_0). \tag{21}$$

For the next iteration step,

$$\underline{a}_1 = \underline{a}_0 - \tau \mathrm{D}_a j(\underline{a}_0) \tag{22}$$

is the improved value for the design variable $\underline{a}$, where $\tau > 0$ is the step length.

In Eq. (19), the partial derivatives $\delta_a J$ and $\partial_s J$ can be easily computed from the definition of J (Eq. (17)); the direct evaluation of $\mathrm{D}_a \underline{s}$ by finite difference approximations, however, requires the numerical solution $\underline{s}$ of Eq. (18) for the variation of each component of the design variable vector $\underline{a}$ in every iteration step. In the shape optimization problem of this work where the number of design variables is large (>1200) and the equality constraint is a partial differential equation, directly calculating $\mathrm{D}_a \underline{s}$ by finite difference method is time consuming. This problem can be circumvented by introducing the Lagrangian

$$L(\underline{a}, \underline{s}, \underline{\lambda}) = J(\underline{a}, \underline{s}) + \underline{\lambda}^{\mathrm{T}} \cdot \underline{R}(\underline{a}, \underline{s}) \tag{23}$$

with a Lagrange multiplier $\underline{\lambda}$. The partial derivatives of the Lagrangian with respect to the state variable $\underline{s}$ and the Lagrange multiplier $\underline{\lambda}$ yield the following equations necessary for the numerical determination of $\mathrm{D}_a j(\underline{a}_0)$:

1. The state equation

$$\partial_\lambda L = \underline{0} \Rightarrow \underline{R}(\underline{a}, \underline{s}) = \underline{0}, \tag{24}$$

   with numerical solution $\underline{s}_0$ for given $\underline{a}_0$.
2. The adjoint equation

$$\partial_s L = \underline{0} \Rightarrow \partial_s J + \underline{\lambda}^{\mathrm{T}} \cdot \partial_s \underline{R} = \underline{0}, \tag{25}$$

$$\text{or } (\partial_s \underline{R})^{\mathrm{T}} \cdot \underline{\lambda} = -(\partial_s J)^{\mathrm{T}}, \tag{26}$$

   with numerical solution $\underline{\lambda}_0$, when $\underline{a}_0$ and the corresponding state variable $\underline{s}_0$ are known.

The gradient of the reduced objective function

$$j(\underline{a}) = J(\underline{a}, \underline{s}(\underline{a})) = L(\underline{a}, \underline{s}(\underline{a}), \underline{\lambda}(\underline{a})) \tag{27}$$

is formally given as

$$\mathrm{D}_a j = \partial_a L + \partial_s L \cdot \mathrm{D}_a \underline{s} + \partial_\lambda L \cdot \mathrm{D}_a \underline{\lambda}. \tag{28}$$

Substituting $\underline{s}_0$ and $\underline{\lambda}_0$ into Eq. (28), the terms $\partial_s L$ and $\partial_\lambda L$ vanish according to Eqs. (25) and (24). Hence, the reduced gradient at $\underline{a}_0$ is given as

$$\mathrm{D}_a j(\underline{a}_0) = \partial_a L(\underline{a}_0, \underline{s}_0, \underline{\lambda}_0) = \partial_a J(\underline{a}_0, \underline{s}_0) + \underline{\lambda}_0^{\mathrm{T}} \cdot \partial_a \underline{R}(\underline{a}_0, \underline{s}_0). \tag{29}$$

This procedure only requires the solution of two equations (Eqs. (24) and (26)) during each iteration step.

As shown by Lions (1968) and Céa (1986), the adjoint method is also applicable to the continuous case as carried out in Section 3.2.

3. Tool design procedure by adjoint-based shape optimization

3.1. Dimensionless formulation of the shape optimization problem

To establish a model describing the key characteristics of the tool design problem and to avoid studies using redundant parameter variations (e.g. doubling $\tilde{U}$ and halving $\tilde{\kappa}$) which produce the same results, the governing equations of the model are made dimensionless, following the approach of Narayanan et al. (1986). For a given gap geometry and set of machining parameters $\tilde{U}$, $\tilde{v}_{\mathrm{f}}$, $\tilde{\kappa}$, and $\tilde{K}_{\mathrm{V}}$ used in an ECM process, the corresponding dimensionless model problem is obtained by normalizing the lengths of the geometry and spacial differential operators by the standard equilibrium front gap $\tilde{h}_{\mathrm{e}}^{\mathrm{std}}$ (cf. Eq. (10)), and the electrical potential by the machining voltage $\tilde{U}$. Using dimensionless variables and differential operators

$$\underline{x} = \frac{1}{\tilde{h}_{\mathrm{e}}^{\mathrm{std}}} \tilde{\underline{x}}, \quad \underline{\nabla} = \tilde{h}_{\mathrm{e}}^{\mathrm{std}} \tilde{\underline{\nabla}}, \quad \Phi = \tilde{\Phi} \big/ \tilde{U}. \tag{30}$$

the dimensionless formulation of the inverse problem (Eqs. (12)–(16)) is given by

$$\underline{\nabla} \cdot (\underline{\nabla} \Phi) = 0 \quad \text{in } \Omega \tag{31}$$

$$\frac{\partial \Phi}{\partial n} = 0 \quad \text{on } \Gamma_{\mathrm{N}} \tag{32}$$

$$\Phi = 0 \quad \text{on } \Gamma_{\mathrm{C}} \text{ (shape unknown)} \tag{33}$$

$$\Phi - 1 = 0 \quad \text{on } \Gamma_{\mathrm{A}} \tag{34}$$

$$\frac{\partial \Phi}{\partial n} - \cos\theta = 0 \quad \text{on } \Gamma_{\mathrm{A}}, \tag{35}$$

which is a partially overdetermined (free boundary) problem (Fragalà and Gazzola, 2008) since both Dirichlet and Neumann boundary conditions are applied to the workpiece boundary Γ_{A}. The tool boundary Γ_{C} is underdetermined due to its unknown shape. Details of the dimensionless calculation domain and the associated boundaries and geometrical quantities are shown in Fig. 2.

The approach used in this work is to reformulate the inverse problem (Eqs. (31)–(35)) into a constrained shape optimization problem (cf. Sokołowski and Zolésio, 1992; Eppler and Harbrecht, 2012) where an initial guess Γ_{C0} is assumed as the shape of the tool. On the overdetermined boundary Γ_{A}, the Neumann boundary condition (Eq. (35)) is transformed into an objective function to be minimized, subject to an equality constraint represented by a boundary value problem posed on Ω. The aim is to find the shape of Γ_{C} that minimizes the objective function

$$\frac{1}{2} \int_{\Gamma_{\mathrm{A}}} \left(\frac{\partial \Phi}{\partial n} - \cos\theta \right)^2 \mathrm{d}S \tag{36}$$

as an integral over the known boundary Γ_{A}, where the electric potential Φ has to satisfy

$$\underline{\nabla} \cdot (\underline{\nabla} \Phi) = 0 \quad \text{in } \Omega \tag{37}$$

$$\frac{\partial \Phi}{\partial n} = 0 \quad \text{on } \Gamma_{\mathrm{N}} \tag{38}$$

$$\Phi = 0 \quad \text{on } \Gamma_{\mathrm{C}} \tag{39}$$

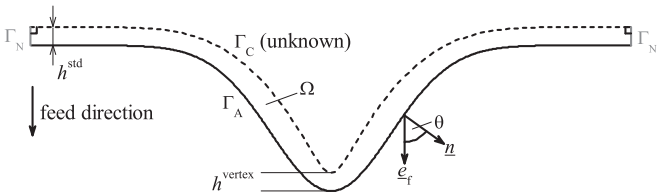

Fig. 2. Details of the inter-electrode gap as calculation domain Ω of the dimensionless ECM tool design model problem (cf. Section 3.1). The workpiece (anode) boundary Γ_{A} is represented by the black solid line. The side boundary Γ_{N}, represented by the gray solid lines, is an auxiliary boundary and does not correspond to any physical surface; it is chosen to be straight lines (in 2D) or planes (in 3D) intersecting Γ_{C} perpendicularly, which will be important in Appendix B. The black dashed line represents the unknown tool (cathode) boundary Γ_{C}. The variable h^{std} denotes the relative width of the (current) standard front gap width $\tilde{h}^{\mathrm{std}}$ with respect to its equilibrium value $\tilde{h}_{\mathrm{e}}^{\mathrm{std}}$, $h^{\mathrm{vertex}} = \tilde{h}^{\mathrm{vertex}} / \tilde{h}_{\mathrm{e}}^{\mathrm{std}}$ is the relative width of the front gap at the anode vertex.

$$\Phi = 1 \quad \text{on } \Gamma_A. \tag{40}$$

During the optimization process, the shape of Γ_C is changed iteratively to minimize the objective function.

3.2. Solution of the shape optimization problem

In the shape optimization problem defined by Eqs. (36)–(40), the objective function (Eq. (36)) is a so-called *shape functional*, i.e. a functional of the domain Ω, namely

$$\Omega \mapsto j(\Omega) = J(\Omega, \Phi) = \frac{1}{2}\int_{\Gamma_A} \left(\frac{\partial \Phi}{\partial n} - \cos\,\theta\right)^2 \mathrm{d}S, \tag{41}$$

where the function $\Phi : \Omega \to \mathbb{R}$ plays the role of a state variable. The equality constraint is defined by the boundary value problem (Eqs. (37)–(40)). The Lagrangian is given as

$$\begin{aligned} L(\Omega, \Phi, \underline{\lambda}) = {} & \frac{1}{2}\int_{\Gamma_A} \left(\frac{\partial \Phi}{\partial n} - \cos\,\theta\right)^2 \mathrm{d}S \\ & + \int_\Omega \lambda_\Omega \underline{\nabla} \cdot (\underline{\nabla}\Phi)\,\mathrm{d}V + \int_{\Gamma_N} \lambda_N \frac{\partial \Phi}{\partial n}\,\mathrm{d}S \\ & + \int_{\Gamma_C} \lambda_C \Phi\,\mathrm{d}S + \int_{\Gamma_A} \lambda_A(\Phi - 1)\,\mathrm{d}S, \end{aligned} \tag{42}$$

where $\underline{\lambda} = (\lambda_\Omega, \lambda_N, \lambda_C, \lambda_A)^T$ denotes the vector of Lagrange multipliers consisting of scalar-valued functions defined in Ω and on the boundaries, respectively.

To obtain the adjoint equation, the partial derivatives with respect to the state variable in the finite dimensional case (Eq. (25)) are replaced by the Gâteaux derivative with respect to Φ in an arbitrary direction ψ

$$\partial_\Phi L(\Omega, \Phi, \underline{\lambda})[\psi] = \lim_{\varepsilon \to 0} \frac{L(\Omega, \Phi + \varepsilon\psi, \underline{\lambda}) - L(\Omega, \Phi, \underline{\lambda})}{\varepsilon}. \tag{43}$$

As shown in Appendix A, the adjoint equation resulting from $\partial_\Phi L(\Omega, \Phi, \underline{\lambda})[\psi] = 0$ (cf. Eq. (25) for the finite dimensional case) is a boundary value problem for λ_Ω, namely (cf. Eqs. (A.6)–(A.9))

$$\nabla \cdot (\nabla \lambda_\Omega) = 0 \quad \text{in } \Omega \tag{44}$$

$$\frac{\partial \lambda_\Omega}{\partial n} = 0 \quad \text{on } \Gamma_N \tag{45}$$

$$\lambda_\Omega = 0 \quad \text{on } \Gamma_C \tag{46}$$

$$\lambda_\Omega = -\left(\frac{\partial \Phi}{\partial n} - \cos\,\theta\right) \quad \text{on } \Gamma_A. \tag{47}$$

To obtain the gradient of the objective function with respect to the design variable, which is the shape of the boundary Γ_C in this case, we use the perturbation method of shape calculus explained in more detail by e.g. Murat and Simon (1976), Pironneau (1984) or Sokołowski and Zolésio (1992). We consider the change in the objective function when the domain Ω is deformed into

$$\Omega_\varepsilon = \{\underline{x} + \varepsilon \underline{v}(\underline{x}); \underline{x} \in \Omega\}, \tag{48}$$

where $\underline{v}$ is the "shape variation velocity field", a Lipschitz-continuous vector field indicating the direction of the infinitesimal movement of each point of Ω to realize a shape variation. The so-called *shape derivative* of an objective shape functional J at Ω in direction $\underline{v}$ is defined as the Eulerian derivative (e.g. Sokołowski and Zolésio, 1992)

$$\partial_\Omega J(\Omega, \Phi)[\underline{v}] = \lim_{\varepsilon \to 0} \frac{J(\Omega_\varepsilon, \Phi) - J(\Omega, \Phi)}{\varepsilon}. \tag{49}$$

As shown in Appendix B, the shape derivative of the Lagrangian is used to calculate the change in the reduced objective function $j(\Omega)$ (Eq. (41)) due to an infinitesimal deformation of the domain Ω (cf. Eq. (48)). As the result, we obtain (cf. Eq. (B.7))

$$\begin{aligned} \mathrm{D}_\Omega j(\Omega)[\underline{v}] &= \partial_\Omega L(\Omega, \Phi, \underline{\lambda})[\underline{v}] \\ &= \int_{\Gamma_C} (\underline{v} \cdot \underline{n}) \frac{\partial \lambda_\Omega}{\partial n} \frac{\partial \Phi}{\partial n}\,\mathrm{d}S, = \int_{\Gamma_C} v_n G\,\mathrm{d}S \end{aligned} \tag{50}$$

where $v_n = \underline{v} \cdot \underline{n}$ is the component of the shape variation velocity field in the direction normal to the boundary Γ_C, and

$$G = \left.\frac{\partial \lambda_\Omega}{\partial n} \frac{\partial \Phi}{\partial n}\right|_{\Gamma_C} \tag{51}$$

is the so-called *shape gradient* (cf. Schmidt et al., 2011). For optimization using the steepest descent method, the optimal search direction is the direction of the negative gradient (cf. Eq. (21)), i.e.

$$\underline{v}^{\mathrm{opt}} \parallel -G\underline{n} \quad \text{or} \quad v_n^{\mathrm{opt}} \propto -G. \tag{52}$$

Hence, each point $\underline{x}$ on Γ_C is moved according to

$$\underline{x} \to \underline{x} - \tau \frac{\partial \lambda_\Omega(\underline{x})}{\partial n} \frac{\partial \Phi(\underline{x})}{\partial n} \underline{n}(\underline{x}) \tag{53}$$

in an iteration step with step length $\tau > 0$.

3.2.1. Numerical implementation

The cathode design procedure described in Section 3.2 is implemented in the freely available open source C++ library OpenFOAM®, which offers object-oriented implementations of differential operators and uses finite volume discretization (Jasak et al., 2007). In this software environment, the implementation of the adjoint equation derived from the continuous approach is straightforward, as discussed by Othmer et al. (2007) for topology optimization of duct flows. In this work, both the state equation ((Eqs. (37)–(40)) and the adjoint equation (Eqs. (44)–(47)) are discretized by applying the central-difference scheme (Patankar, 1980, Section. 5.21). The resulting linear equation systems involving symmetrical coefficient matrices are solved using the conjugate gradient method. After calculation of the shape derivative according to Eq. (49), the tool boundary Γ_C is moved according to Eq. (53).

To propagate the boundary motion to the mesh interior, we use the approach described by Löhner and Yang (1996): the mesh motion velocity is determined as the solution of a Laplace equation with the boundary motion velocities as boundary conditions. In our case, the boundary Γ_A is fixed, Γ_N does not move in the normal direction; the boundary velocity at Γ_C is given by $-G\underline{n}$ (cf. Eq. (52)). The motion velocity equation is discretized using the finite volume method and then solved; the obtained velocity values in the cell centers have to be linearly interpolated to the mesh points which are moved before the next iteration starts. So far, we have applied this mesh motion procedure due to its simple implementation, as the available numerical schemes can be re-used. For our studies, the accuracy of this method is sufficient (cf. Section 4); however, according to a study of Jasak and Tuković (2006) this kind of "cell-based" method could sometimes lead to degenerating cells and should be replaced by a "point-based" solution for the motion equation in those cases.

To evaluate the convergence of the optimization process, two "indicators" are calculated at the end of each iteration step, namely the maximum-norm of the shape gradient (cf. Eq. (51))

$$G_{\max} = \max_{\Gamma_C} \left|\frac{\partial \lambda_\Omega}{\partial n} \frac{\partial \Phi}{\partial n}\right|, \tag{54}$$

and the quantity

$$\delta_{\max} = \max_{\Gamma_A} \left| \frac{1}{\cos\theta} \frac{\partial \Phi}{\partial n} - 1 \right| \tag{55}$$

which is derived from the integrand of the objective function (cf. Eq. (41)). The necessary condition for a local extremum in optimization is a zero gradient, i.e. $G_{\max} = 0$; furthermore, the value of $G_{\max}$ is used to assess whether additional iteration steps would further "improve" the tool shape substantially. However, a zero gradient is not sufficient to assess whether the obtained tool shape Γ_C is a solution of the original inverse problem (Eqs. (31)–(35)), i.e. whether the condition on the over-determined workpiece boundary (Eq. (35)) is fulfilled; this will be the case when the non-negative quantity $\delta_{\max}$ is zero. Hence, both quantities, $G_{\max}$ and $\delta_{\max}$, are taken into account to decide when to stop the iteration process.

4. Results and discussion

In this section, the implemented solver is applied to tool design for selected 2D and 3D workpiece shapes.

To assess the accuracy of the tool design method described in Section 3.2, we first choose 2D workpiece geometries in x–z plane described by a series of Gaussians

$$z_A = -A \exp\left(-\frac{x_A^2}{2\sigma^2}\right), \quad |x_A| \le 15 \tag{56}$$

for which exact tool shapes as analytical solutions in parametric form

$$x_C(t) = t - A \exp\left[\frac{1-t^2}{2\sigma^2}\right] \sin\left(\frac{t}{\sigma^2}\right), \tag{57}$$

$$z_C(t) = 1 - A \exp\left[\frac{1-t^2}{2\sigma^2}\right] \cos\left(\frac{t}{\sigma^2}\right), \tag{58}$$

can be derived applying the complex variable method presented by Nilson and Tsuei (1974).

As an example, Fig. 3 illustrates the specification and the solution of a two-dimensional tool design problem for the workpiece shape described by a Gaussian with parameters $A=8$ and $\sigma=4$ (black dashed line in panel (a)), which is the shape with the largest curvature and thus most challenging among all 2D geometries studied in this work. For the iterative tool design process, it is reasonable to start with an initial tool shape Γ_{C0} corresponding to the offset curve of the workpiece surface with fixed normal distance 1 in the normalized problem (dotted black line in Fig. 3(a)). In this case, plane regions of Γ_{C0} for which $\theta = 0$ already satisfy the condition of a valid tool (Eq. (35)). The calculation domain is divided into 200 cells in the direction along and 20 in the direction across the gap. At the end of each iteration, the tool geometry is moved according to Eq. (53) with step length $\tau = 0.4$. In the following iteration, the state and the adjoint equation are solved again for the improved tool shape.

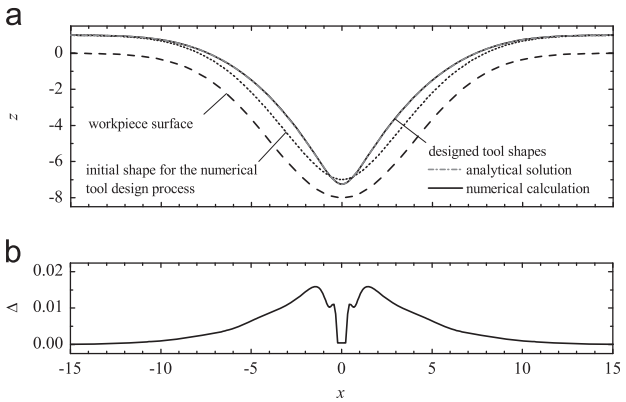

Fig. 3. Two-dimensional tool design example. Lengths in x and z direction are normalized to the standard equilibrium front gap width $\tilde{h}_e^{std}$ according to Eq. (30). In panel (a), the black dashed line shows the workpiece shape defined by Eq. (56) with $A=8$ and $\sigma=4$; the geometry of the tool at the beginning of the tool design iteration is represented by the dotted black line obtained from equidistantly offsetting the workpiece surface by 1; the tool shape obtained from iterative optimization (black solid line) overlaps with the analytical solution (gray dash-dotted line) obtained from Eqs. (57) and (58). Panel (b) shows the deviation Δ of the numerical optimization result from the analytical solution in normal direction.

During the optimization process, the "convergence indicators" $G_{\max}$ and $\delta_{\max}$ are calculated in each iteration and their evolution is visualized on line. As illustrated in Fig. 4(a), the value of $G_{\max}$ decreases from initially 0.36 to 1.3×10^{-4} after 200 iterations, the value of $\delta_{\max}$ decreases from 0.57 to 1.2×10^{-3} after the same number of iterations (Fig. 4(b)). The tool shape obtained after 200 iterations is shown by the dash-dotted gray line in Fig. 3(a) which overlaps with the analytical solution according to Eqs. (57) and (58) (solid black line) on this scale. Hence, the absolute deviation Δ between these solutions in surface normal direction is calculated and shown in Fig. 3(b). The maximum of Δ is found at $x = \pm 1.5$ and its value $\Delta_{\max}$ is less than 2% of the width of the standard equilibrium front gap. To evaluate the evolution of the actual accuracy, $\Delta_{\max}$ is determined for the tool shape obtained after every iteration step and plotted as a function of the iteration number. As shown in Fig. 4(c), $\Delta_{\max}$ remains constant after 120 iteration steps. As further studies (not shown here) reveal, the value of $\Delta_{\max}$ after 200 iteration steps can be reduced further by increasing the number of cells in the direction across the gap. However, since the gap in ECM is usually of the order of 100 μm, a deviation of $\Delta_{\max} < 0.02$ corresponds to the same order of magnitude as the typical manufacturing tolerance for the tool. Hence, for all other calculations in this work, the domain is divided into 20 cells in the direction across the gap. Using a 200×20 mesh, the calculation shown in Fig. 3 takes 11.3 s for 200 iteration steps on a single Intel Xeon X5550 processor (2.67 GHz).

The tool design procedure is further applied to a series of axisymmetric 3D geometries described by Gaussian surfaces

$$z_A = -A \exp\left(-\frac{x_A^2 + y_A^2}{2\sigma^2}\right). \tag{59}$$

As initial shape of the tool, an offset surface of the workpiece with fixed vertical distance of 1 is constructed. The interelectrode gap as calculation domain is divided into 200 cells in each of the horizontal directions and 20 in the vertical direction. Fig. 5 shows the results of the tool design procedure for the workpiece shape defined by Eq. (59) with $A=8$ and $\sigma=4$.

In the following, we use the results of a series of 2D and 3D tool shape calculations to discuss the influence of the curvature of the workpiece vertex (tip at $x=y=0$) on the equilibrium front gap in tool design. As can be seen in Figs. 3 and 5, the equilibrium front gap width h_e^{vertex} at the vertex of the electrodes is smaller than the standard equilibrium gap h_e^{std} which would result from tool design using the $\cos\theta$–method (cf. positions of h^{vertex} and h^{std} in Fig. 2). In both examples, the workpiece surface is described by a convex function in the vicinity of the vertex. In Fig. 6, designed tool shapes corresponding to 2D and 3D workpiece shapes with $A=8$ are compared with those corresponding to $A=-8$ to illustrate the influence of curvature of the electrodes on h_e^{vertex}, the equilibrium front gap width at the electrode vertex. For workpiece shapes with $A=8$, which are convex in the vicinity of the vertex (Fig. 6(a)), the values of h_e^{vertex} obtained from shape optimization are 0.73 in the 2D case and 0.61 in the 3D case, which deviate from the value 1 ($\cos\theta$–method) by 27% and 39%, respectively. For the concave workpiece shapes ($A=-8$) shown in Fig. 6(b), the values of h_e^{vertex}

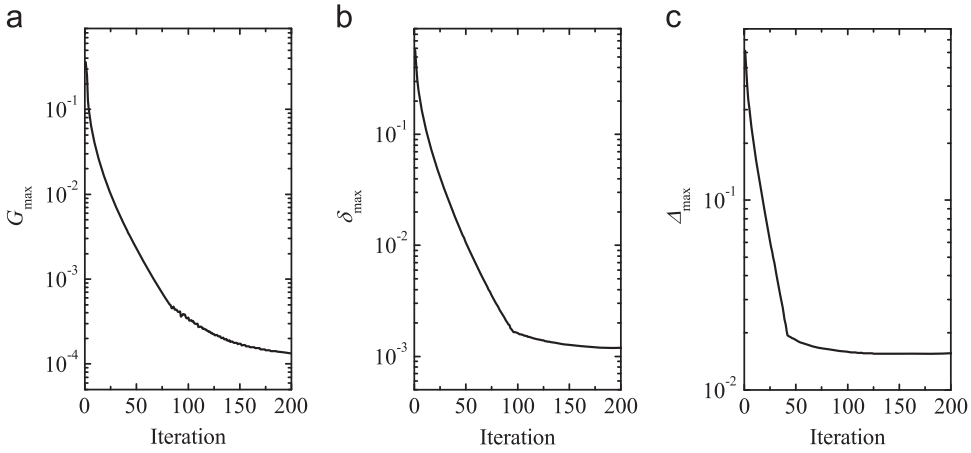

Fig. 4. Evolution of the "convergence indicators" and the actual accuracy during the tool design example of Fig. 3(a) in semi-logarithmic representation. Panel (a) shows the maximum-norm of the shape gradient (Eq. (54)). Panel (b) shows the quantity δ_{max} defined in Eq. (55). Panel (c) illustrates the maximum deviation Δ_{max} of the numerically calculated tool from the exact solution in surface normal direction as a function of the iteration number. The quantities G_{max} and δ_{max} are calculated during the optimization process, the quantity Δ_{max} is evaluated in the post-processing stage.

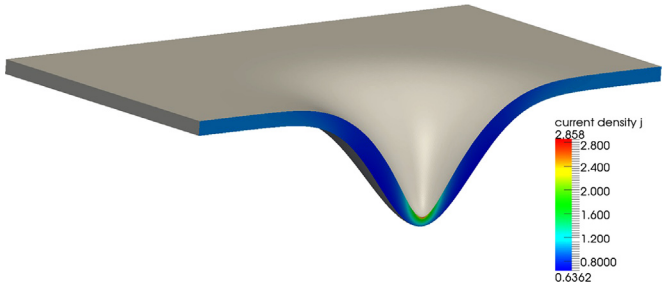

Fig. 5. Three-dimensional tool design example. The upper surface is the designed tool shape corresponding to the prescribed workpiece shape (lower surface) defined by Eq. (59) with $A=8$ and $\sigma=4$. The color map shows the electric current density within a sectional plane through the vertex normalized by its value in the standard equilibrium front gap. (For interpretation of the references to color in this figure legend, the reader is referred to the web version of this article.)

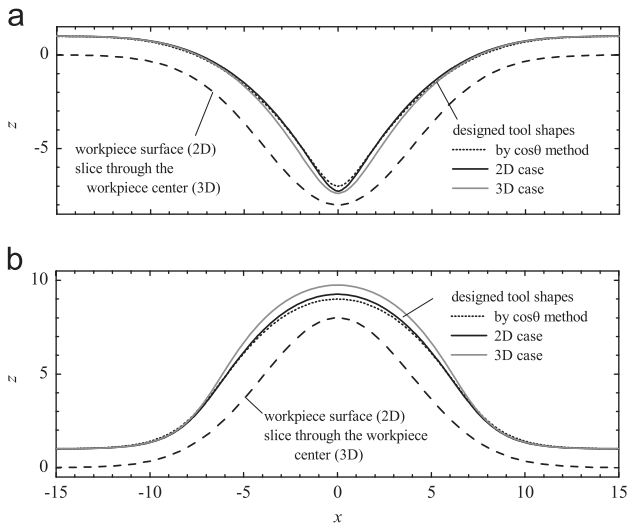

Fig. 6. Cathode shapes designed for 2D anodes compared with those designed for axisymmetric 3D anodes. For the axisymmetric 3D cases, the figure shows a slice though the vertex of the electrodes. Panel (a) illustrates an example in which the electrodes are convex in the vicinity of the vertex. Panel (b) shows an example in which the electrodes are concave in the vicinity of the vertex.

are 1.26 for 2D and 1.74 for 3D, whereas h_e^{vertex} is 1 when employing the cos θ−method for both cases.

The deviations of h_e^{vertex} from the standard equilibrium gap $h_e^{std}=1$ can be made plausible by an analytical approximation

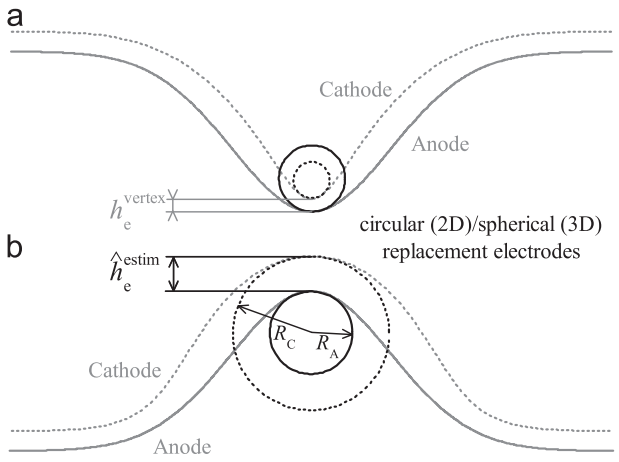

Fig. 7. Approximations of the tool (cathode) and the workpiece (anode) in the vicinity of the vertex in the convex case (a) and in the concave case (b). The radii R_A of the replacement anodes (black solid circles) are equal to the signed curvature radii (cf. Eq. (62)) of the prescribed anodes (gray solid lines) a the vertex. The replacement cathodes (black dashed circles of radii R_C) are assumed to be concentric to the replacement anodes. The equilibrium front gap width at the electrode vertex is denoted h_e^{vertex} which is estimated by $\hat{h}_e^{estim}$, the difference between R_A and R_C.

model, where the tool (cathode) and the workpiece (anode) are approximated by "replacement electrodes" consisting of concentric circles or spheres in the vicinity of the vertex, as illustrated in Fig. 7. The estimate $\hat{h}_e^{estim}$ of the equilibrium front gap at the vertex h_e^{vertex} is the difference between the radius of the replacement anode R_A and that of the replacement cathode R_C. As shown in Appendix D, the Laplace equation is solved in the domain between the replacement electrodes to obtain the electric potential distribution; $\hat{h}_e^{estim}$ is determined by the steady state machining condition (Eq. (35)) that the solution has to satisfy additionally. For 2D cases, h_e^{vertex} is estimated by Eq. (D.3), i.e.

$$\hat{h}_e^{estim} = R_A(1-e^{-1/R_A}), \tag{60}$$

and for 3D cases, it is estimated by Eq. (D.5), i.e.

$$\hat{h}_e^{estim} = \frac{1}{1+1/R_A}, \tag{61}$$

where the (signed) radius of curvature of the workpiece surface

$$R_A = \frac{\sigma^2}{A} \tag{62}$$

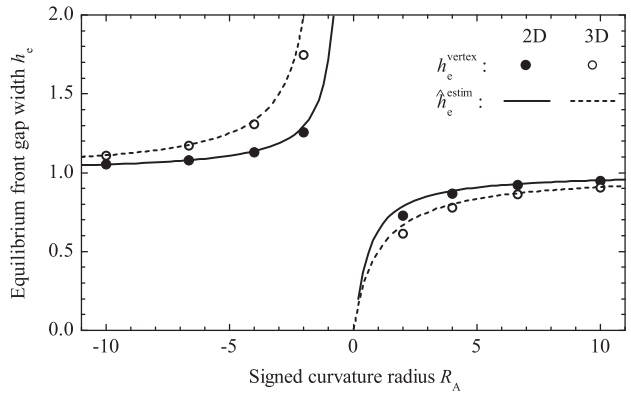

Fig. 8. Equilibrium front gap width at the vertex as a function of the signed curvature radius for 2D (solid lines and full symbols) and 3D (dashed lines and open symbols) cases. The values h_e^{vertex} obtained from the tool design procedure (symbols) are compared with the results of the analytical approximation model (lines) according to Eqs. (60) and (61).

is obtained from Eqs. (56) and (59) at $x_A = y_A = 0$. The radius of curvature R_A is positive for workpiece shapes which are convex in the vicinity of the vertex ($A > 0$; Fig. 7(a)) and negative for workpiece shapes which are concave in the vicinity of the vertex ($A < 0$; Fig. 7(b)).

The tool design procedure is applied to workpiece shapes with R_A values of ± 2, ± 4, ± 6.67, and ± 10 for both 2D and 3D cases. The results are compared with the analytical estimate and shown in Fig. 8. The analytical estimate of the equilibrium front gap at the vertex for this study is higher than the values obtained from shape optimization. The relative deviations of the results are below 8% except for the value 14% obtained for $R_A = -2$, and decrease with increasing $|R_A|$. The estimated value $\hat{h}_e^{estim}$ deviates more significantly from h_e^{vertex} for small $|R_A|$ since the osculating circles or spheres of tool and workpiece surfaces are not exactly concentric.

5. Conclusion

The tool design problem in electrochemical machining can be reformulated as a shape optimization problem with the positions of the tool boundary points as design variables and an integral over the workpiece boundary as objective functional. The reduced gradient of the objective function can be efficiently calculated by solving the state and the adjoint equation combined with the use of shape derivatives. Applying the shape optimization method, the tool designed for a two dimensional Gaussian-shaped workpiece deviates from the exact analytical solution by less than the engineering tolerance. The method can be applied to design appropriate tools corresponding to three dimensional Gaussian-shaped workpieces. The cos θ−method is shown to be inaccurate for the estimate of the front gap width in the case of curved electrode surfaces. This inaccuracy can be estimated by the analytical approximation model derived in this work. For future projects, the method developed in this work could be extended, e.g. to the design of ECM tools corresponding to more general workpiece shapes or by incorporation of further effects such as non-uniform electrolyte conductivity. Research groups who have already developed complex ECM process simulations could include the presented concept in their models to design tools under more realistic conditions.

Nomenclature

Abbreviations

2D, 3D	two-, three-dimensional
BEM	boundary element method
ECM	electrochemical machining
FEM	finite element method
FVM	finite volume method

Symbols, over and undersets

$\tilde{\cdot}$ (tilde)	dimensioned physical quantity
$\underline{\cdot}$ (underline)	vector quantity or operator
$\underline{\nabla}$	nabla operator
$\partial(\cdot)/\partial n$	normal derivative on a boundary
$\partial_x(\cdot)$	partial derivative with respect to x
$\partial_\Phi L(\cdot, \Phi_0)[\psi]$	Gâteaux derivative of L with respect to Φ at Φ_0 in direction ψ
$\partial_\Omega J(\Omega_0, \cdot)[\underline{v}]$	partial shape derivative of J at Ω_0 in the direction of the shape variation velocity field $\underline{v}$
$\mathrm{D}_x(\cdot)$	total derivative with respect to x
$\mathrm{D}_{\underline{a}} j(\underline{a}_0)[\underline{v}]$	directional derivative of j with respect to $\underline{a}$ at $\underline{a}_0$ in direction $\underline{v}$
$\mathrm{D}_\Omega j(\Omega_0)[\underline{v}]$	total shape derivative of the reduced objective function j at Ω_0 in direction of the shape variation velocity field $\underline{v}$
$\parallel$	parallel
$(\cdot)^T$	transposed
$\mathbb{R}$	the set of all real numbers
$\mathbb{C}$	the set of all complex numbers
$\mathcal{O}$	order of

Upper-case roman

A	height of the Gaussian function
$F(x)$	real analytic function
$\hat{F}(z)$	complex analytic continuation of $F(x)$
$\tilde{F}$	Faraday constant $\tilde{F} = 96485$ As/mol
G, (G_{max})	(maximum) shape gradient
$\tilde{I}$	total electric current
J, $J(\underline{a}, \underline{s})$	objective function(al)
$\tilde{K}_V$	machining constant $\tilde{K}_V = \tilde{M}/(\tilde{\rho} z \tilde{F})$
L	Lagrangian
$\tilde{M}$	molar mass of the anode metal
$\underline{R}$	expressions of equality constraints
R_A	signed curvature radius of the anode at its vertex
R_{in}, R_{out}	radius of the inner and outer replacement electrode
$\dot{\tilde{V}}$	volume dissolution rate
$\tilde{U}$	machining voltage

Lower-case roman

$\underline{a}$	vector of design variables
$\underline{e}_f$	unit vector in feed direction
$\hat{h}_e^{estim}$	estimated equilibrium gap width
$\tilde{h}^{std}$, (h^{std})	(dimensionless) standard front gap width
$\tilde{h}_e^{std}$	standard equilibrium front gap width
h_e^{vertex}	equilibrium front gap width at electrode vertex
j, $j(\underline{a})$	reduced objective function
$\underline{\tilde{j}}$	current density

$\tilde{j}_A$	current density at anode surface
$\underline{n}$	outer unit normal of anode boundary
$\underline{s}$, $\underline{s}(\underline{a})$	vector of state variables
t	curve parameter
$\tilde{t}$	time
$\underline{v}$	search direction (finite dimensional), shape variation velocity field (continuous)
v_n	component of shape variation velocity field in boundary normal direction
$\tilde{\underline{v}}_A$	anode dissolution velocity
$\tilde{\underline{v}}_f$, $(\tilde{v}_f)$	(magnitude of) cathode feed velocity
$\tilde{\underline{x}}$, $(\underline{x})$	(dimensionless) spacial coordinate
$x_{A,C}$, $y_{A,C}$, $z_{A,C}$	coordinates of points on cathode and anode boundaries
z	valency of the anode metal

Upper-case greek

Γ	boundary (in general)
$\tilde{\Gamma}_A$, (Γ_A)	(dimensionless) anode boundary
$\tilde{\Gamma}_C$, (Γ_C)	(dimensionless) cathode boundary
$\tilde{\Gamma}_N$, (Γ_N)	(dimensionless) non-metallic side boundary
Δ, (Δ_{max})	(maximum) deviation of the numerically calculated tool surface from the exact solution in surface normal direction
$\tilde{\Phi}$, (Φ)	(dimensionless) electric potential
$\tilde{\Omega}$, (Ω)	(dimensionless) calculation domain
$\partial\Omega$	total boundary of the dimensionless calculation domain
Ω_ε	deformed calculation domain

Lower-case greek

δ_{max}	convergence indicator defined by Eq. (55)
θ	angle between the feed direction and the outer normal of the anode boundary
$\tilde{\kappa}$	electrolyte conductivity
$\underline{\lambda}$	vector of Lagrange multipliers
$\lambda_{\Omega,A,C,N}$	Lagrange multipliers for calculation domain, anode, cathode and non-metallic side boundary
$\tilde{\rho}$	anode metal mass density
σ	standard deviation of the Gaussian
τ	iteration step length
ψ	direction in function space

Acknowledgements

The authors would like to express their gratitude to Prof. G.A. Francfort (Université Paris 13, France) and Prof. A. Henrot (École des Mines de Nancy, France) for valuable discussions and suggestions.

Appendix A. Derivation of the adjoint equations

For the Gâteaux derivative (Eq. (43)) of the Lagrangian (Eq. (42)) with respect to Φ in an arbitrary direction ψ, we obtain

$$\begin{aligned}\partial_\Phi L(\Omega,\Phi,\underline{\lambda})[\psi] = &\int_{\Gamma_A}\left(\frac{\partial\Phi}{\partial n}-\cos\theta\right)\frac{\partial\psi}{\partial n}\,dS\\ &+\int_\Omega \lambda_\Omega\underline{\nabla}\cdot(\underline{\nabla}\psi)\,dV+\int_{\Gamma_N}\lambda_N\frac{\partial\psi}{\partial n}dS\\ &+\int_{\Gamma_C}\lambda_C\psi\,dS+\int_{\Gamma_A}\lambda_A\psi\,dS.\end{aligned}\tag{A.1}$$

Applying the identity

$$\lambda\underline{\nabla}\cdot(\underline{\nabla}\psi)=\psi\underline{\nabla}\cdot(\underline{\nabla}\lambda)+\underline{\nabla}\cdot(\lambda\underline{\nabla}\psi-\psi\underline{\nabla}\lambda)\tag{A.2}$$

and the divergence theorem

$$\int_\Omega \underline{\nabla}\cdot(\lambda\underline{\nabla}\psi)\,dV=\int_{\partial\Omega}\lambda\frac{\partial\psi}{\partial n}\,dS,\tag{A.3}$$

Eq. (A.1) can be recast into

$$\begin{aligned}\partial_\Phi L(\Omega,\Phi,\underline{\lambda})[\psi] = &\int_{\Gamma_A}\left(\frac{\partial\Phi}{\partial n}-\cos\theta\right)\frac{\partial\psi}{\partial n}\,dS\\ &+\int_\Omega \underline{\nabla}\cdot(\underline{\nabla}\lambda_\Omega)\psi\,dV+\int_{\partial\Omega}\left(\lambda_\Omega\frac{\partial\psi}{\partial n}-\psi\frac{\partial\lambda_\Omega}{\partial n}\right)dS\\ &+\int_{\Gamma_N}\lambda_N\frac{\partial\psi}{\partial n}\,dS+\int_{\Gamma_C}\lambda_C\psi\,dS+\int_{\Gamma_A}\lambda_A\psi\,dS.\end{aligned}\tag{A.4}$$

After splitting up the surface integral over the whole boundary $\partial\Omega$ into surface integrals over Γ_N, Γ_C and Γ_A, and summarizing the integrands, we obtain

$$\begin{aligned}\partial_\Phi L(\Omega,\Phi,\underline{\lambda})[\psi] = &\int_\Omega[\underline{\nabla}\cdot(\underline{\nabla}\lambda_\Omega)]\psi\,dV\\ &+\int_{\Gamma_N}\left[(\lambda_\Omega+\lambda_N)\frac{\partial\psi}{\partial n}-\left(\frac{\partial\lambda_\Omega}{\partial n}\right)\psi\right]dS\\ &+\int_{\Gamma_C}\left[(\lambda_\Omega)\frac{\partial\psi}{\partial n}+\left(\lambda_C-\frac{\partial\lambda_\Omega}{\partial n}\right)\psi\right]dS\\ &+\int_{\Gamma_A}\left[\left(\frac{\partial\Phi}{\partial n}-\cos\theta\right)+\lambda_\Omega\right]\frac{\partial\psi}{\partial n}\,dS\\ &+\int_{\Gamma_A}\left(\lambda_A-\frac{\partial\lambda_\Omega}{\partial n}\right)\psi\,dS.\end{aligned}\tag{A.5}$$

To fulfill $\partial_\Phi L(\Omega,\Phi,\underline{\lambda})[\psi]=0$, which is required to determine the adjoint equation in the continuous case (cf. Eq. (25) for the finite dimensional case), all terms in brackets followed by ψ or $\partial\psi/\partial n$ in Eq. (A.5) have to vanish since ψ is chosen arbitrarily. As a result we obtain the adjoint equation as a boundary value problem (cf. Eqs. (44)–(47))

$$\nabla\cdot(\nabla\lambda_\Omega)=0\quad\text{in }\Omega\tag{A.6}$$

$$\frac{\partial\lambda_\Omega}{\partial n}=0\quad\text{on }\Gamma_N\tag{A.7}$$

$$\lambda_\Omega=0\quad\text{on }\Gamma_C\tag{A.8}$$

$$\lambda_\Omega=-\left(\frac{\partial\Phi}{\partial n}-\cos\theta\right)\quad\text{on }\Gamma_A\tag{A.9}$$

and the relations

$$\lambda_N=-\lambda_\Omega|_{\Gamma_N},\quad \lambda_C=\left.\frac{\partial\lambda_\Omega}{\partial n}\right|_{\Gamma_C},\quad\text{and}\lambda_A=\left.\frac{\partial\lambda_\Omega}{\partial n}\right|_{\Gamma_A}.\tag{A.10}$$

Appendix B. Derivation of the reduced gradient

To calculate the shape derivative (Eq. (49)) of a shape functional $J(\Omega,\Phi)$, basic elements of shape calculus are used. For a volume

integral

$$J_1(\Omega,\Phi)=\int_\Omega f\,\mathrm{d}V,$$

with f being a function that does not explicitly depend on the boundary (e.g. the unit surface normal $\underline{n}$), the shape derivative is given as (Céa, 1986, Eq. (3.8))

$$\partial_\Omega J_1(\Omega,\Phi)[\underline{v}]=\int_{\partial\Omega}(\underline{v}\cdot\underline{n})f\,\mathrm{d}S. \tag{B.1}$$

In the case of a surface integral

$$J_2(\Omega,\Phi)=\int_\Gamma f\,\mathrm{d}V$$

the shape derivative is given as (Céa, 1986, Eq. (3.9))

$$\partial_\Omega J_2(\Omega,\Phi)[\underline{v}]=\int_\Gamma(\underline{v}\cdot\underline{n})\left(\frac{\partial f}{\partial n}+Hf\right)\mathrm{d}S, \tag{B.2}$$

where H is the additive mean curvature of Γ. As indicated by the term $\underline{v}\cdot\underline{n}$ in the integrands of Eqs. (B.1) and (B.2), only the component of the shape variation velocity field $\underline{v}$ in boundary normal direction $\underline{n}$ contributes to the shape derivative; in particular, the shape derivative vanishes for boundaries on which the admissible shape variation velocity field is zero or in tangential direction.

To ensure the differentiability of the shape functional and to preserve the continuity of the total domain boundary $\partial\Omega$, the shape variation velocity field $\underline{v}$ in this work has to satisfy the following boundary conditions:

- The (prescribed) workpiece boundary Γ_A is fixed, i.e. $\underline{v}|_{\Gamma_\mathrm{A}}=\underline{0}$.
- The boundary Γ_C representing the tool to be optimized iteratively can move in the boundary normal direction, i.e. $\underline{v}|_{\Gamma_\mathrm{C}}=v_n\underline{n}$.
- The variation of the (auxiliary) side boundary Γ_N is restricted to its tangential direction. The intersection points of Γ_N with Γ_C are allowed to move with $\underline{v}|_{\Gamma_\mathrm{C}}$, which is consistent since Γ_N and Γ_C are perpendicular to each other in these points (cf. Fig. 2).

Furthermore, the boundaries Γ_C, Γ_N, and Γ_A have to be regular, which is fulfilled in the applications of this work (for a mathematically more precise proof of the differentiability of the shape functional in a similar example, the reader is referred to Kiniger and Vexler, 2013). Taking the boundary conditions for $\underline{v}$ into account, only the terms

$$L_1(\Omega,\Phi,\underline{\lambda})=\int_\Omega\lambda_\Omega\nabla\cdot(\nabla\Phi)\,\mathrm{d}V \tag{B.3}$$

and

$$L_2(\Omega,\Phi,\underline{\lambda})=\int_{\Gamma_\mathrm{C}}\lambda_\mathrm{C}\Phi\,\mathrm{d}S \tag{B.4}$$

can contribute to the shape derivative of the Lagrangian (Eq. (42)). For L_1, application of Eq. (B.1) yields

$$\partial_\Omega L_1[\underline{v}]=\int_{\Gamma_\mathrm{C}}(\underline{v}\cdot\underline{n})[\lambda_\Omega\nabla\cdot(\nabla\Phi)]\,\mathrm{d}S, \tag{B.5}$$

which vanishes since $\lambda_\Omega=0$ on Γ_C (Eq. (46)). For L_2, application of Eq. (B.2) yields

$$\partial_\Omega L_2[\underline{v}]=\int_{\Gamma_\mathrm{C}}(\underline{v}\cdot\underline{n})\lambda_\mathrm{C}\frac{\partial\Phi}{\partial n}\,\mathrm{d}S+\int_{\Gamma_\mathrm{C}}(\underline{v}\cdot\underline{n})\Phi\left(\frac{\partial\lambda_\mathrm{C}}{\partial n}+H\lambda_\mathrm{C}\right)\mathrm{d}S \tag{B.6}$$

where the latter integral vanishes as $\Phi=0$ on Γ_C (Eq. (39)). With $\lambda_\mathrm{C}=\partial\lambda_\Omega/\partial n$ on Γ_C (Eq. (A.10)), the shape derivative of the reduced objective function (Eq. (41)) is given as (cf. Céa, 1986, Eq. (3.23))

$$\mathrm{D}_\Omega j(\Omega)[\underline{v}]=\partial_\Omega L(\Omega,\Phi,\underline{\lambda})[\underline{v}]=\int_{\Gamma_\mathrm{C}}(\underline{v}\cdot\underline{n})\frac{\partial\lambda_\Omega}{\partial n}\frac{\partial\Phi}{\partial n}\,\mathrm{d}S. \tag{B.7}$$

Appendix C. Analytical solution of special 2D ECM tool design problems

The analytical solution used to verify the numerical results is obtained using the method of Nilson and Tsuei (1974). For a desired workpiece shape (in x–z-plane) that can be represented by the graph of a function $F: D\subset\mathbb{R}\to\mathbb{R}; x_\mathrm{A}\mapsto z_\mathrm{A}=F(x_\mathrm{A})$ with analytic complex continuation $\hat{F}:\mathbb{C}\to\mathbb{C}$, the parametric representation of the tool surface is given as (Nilson and Tsuei, 1974, Eq. (26))

$$x_\mathrm{C}(t)=t+\mathrm{Im}[\hat{F}(t-\mathrm{i})]$$

$$z_\mathrm{C}(t)=1+\mathrm{Re}[\hat{F}(t-\mathrm{i})]$$

with curve parameter t. The workpiece shape chosen in this study is defined by the function

$$F(x_\mathrm{A})=-A\exp\left(-\frac{x_\mathrm{A}^2}{2\sigma^2}\right),$$

resulting in the cathode shape given by

$$x_\mathrm{C}(t)=t-A\exp\left(\frac{1-t^2}{2\sigma^2}\right)\sin\left(\frac{t}{\sigma^2}\right),$$

$$z_\mathrm{C}(t)=1-A\exp\left(\frac{1-t^2}{2\sigma^2}\right)\cos\left(\frac{t}{\sigma^2}\right).$$

Appendix D. Analytical estimate of the front gap for ECM using curved electrodes

D.1. 2D case

For the 2D tool design problem with workpiece shapes described by

$$z_\mathrm{A}=-A\exp\left(-\frac{x_\mathrm{A}^2}{2\sigma^2}\right),$$

the analytical estimate of the front gap is derived from the solution of the two-dimensional Laplace equation in a domain between concentrical circles of radii R_out and R_in. For

$$\begin{aligned}&\nabla\cdot(\nabla\Phi)=0 \quad \text{for } R_\mathrm{in}<|\underline{x}|<R_\mathrm{out}\\ &\Phi=U_\mathrm{in} \quad \text{for } |\underline{x}|=R_\mathrm{in}\\ &\Phi=U_\mathrm{out} \quad \text{for } |\underline{x}|=R_\mathrm{out},\end{aligned} \tag{D.1}$$

the solution in the 2D polar coordinate system

$$x=r\cos\varphi,\quad y=r\sin\varphi$$

is given as

$$\Phi=\frac{U_\mathrm{out}\ln(r/R_\mathrm{in})+U_\mathrm{in}\ln(R_\mathrm{out}/r)}{\ln(R_\mathrm{out}/R_\mathrm{in})}$$

with $r=|\underline{x}|$.

For workpiece shapes which are convex in the vicinity of the vertex, i.e. $A>0$ in Eq. (56), the inner circle corresponds to the replacement cathode (cf. Fig. 7(a)). With $U_\mathrm{in}=0$, $U_\mathrm{out}=1$, $R_\mathrm{out}=R_\mathrm{A}$, $R_\mathrm{in}=R_\mathrm{A}-\hat{h}_\mathrm{e}^{\mathrm{estim}}$ and $\theta=0$, the condition for steady state

machining (cf. Eq. (35)) reads

$$\left.\frac{\partial \Phi}{\partial r}\right|_{r=R_{\text{out}}} = \frac{1}{R_A \ln[R_A/(R_A-\hat{h}_e^{\text{estim}})]} = 1. \tag{D.2}$$

For workpiece shapes which are concave in the vicinity of the vertex, i.e. $A<0$ in Eq. (56), the inner circle corresponds to the replacement anode (cf. Fig. 7(b)) with $R_{\text{in}} = -R_A = -\sigma^2/A > 0$. With $U_{\text{in}} = 1$, $U_{\text{out}} = 0$, $R_{\text{out}} = -R_A + \hat{h}_e^{\text{estim}}$, and $\theta = 0$, the condition for steady state machining (cf. Eq. (35))

$$\left.\frac{\partial \Phi}{\partial n}\right|_{\Gamma_A} = -\left.\frac{\partial \Phi}{\partial r}\right|_{r=R_{\text{in}}} = 1$$

reads

$$\frac{1}{(-R_A)\ln[(-R_A+\hat{h}_e^{\text{estim}})/(-R_A)]} = 1,$$

which is exactly the same expression as Eq. (D.2). Solving Eq. (D.2) for $\hat{h}_e^{\text{estim}}$, the analytical estimate of the equilibrium front gap at the vertex is

$$\hat{h}_e^{\text{estim}} = R_A(1-e^{-1/R_A}), \tag{D.3}$$

where

$$R_A = \frac{\sigma^2}{A}$$

is the signed curvature radius at the workpiece vertex. A Taylor series expansion of Eq. (D.3) yields

$$\hat{h}_e^{\text{estim}} = 1 - \frac{1}{2R_A} + \mathcal{O}\left(\frac{1}{R_A^2}\right).$$

In the limit of large $|R_A|$, the equilibrium front gap at the vertex approaches the value of the standard front gap $h_e^{\text{std}} = 1$, as expected from plane electrodes.

D.2. 3D case

For the 3D tool design problem with workpiece shapes described by

$$z_A = -A\exp\left(-\frac{x_A^2+y_A^2}{2\sigma^2}\right),$$

the solution of Eq. (D.1) in a domain between concentrical spheres of radii R_{out} and R_{in} in a 3D spherical coordinate system is

$$\Phi = \frac{U_{\text{in}}(1/r-1/R_{\text{out}}) + U_{\text{out}}(1/R_{\text{in}}-1/r)}{1/R_{\text{in}}-1/R_{\text{out}}}$$

with $r = |\underline{x}|$. For workpiece shapes which are convex in the vicinity of the vertex, i.e. $A>0$ in Eq. (56), the inner sphere corresponds to the replacement cathode (cf. Fig. 7(a)). With $U_{\text{in}} = 0$, $U_{\text{out}} = 1$, $R_{\text{out}} = R_A$, $R_{\text{in}} = R_A - \hat{h}_e^{\text{estim}}$ and $\theta = 0$, the condition for steady state machining (cf. Eq. (35)) reads

$$\left.\frac{\partial \Phi}{\partial r}\right|_{r=R_{\text{out}}} = \frac{R_A(R_A-\hat{h}_e^{\text{estim}})}{R_A-(R_A-\hat{h}_e^{\text{estim}})}\frac{1}{R_A^2} = 1. \tag{D.4}$$

Similar to the analysis of the 2D problem for $A<0$, the condition for steady state machining yields the same equation as obtained for the case $A>0$. Solving Eq. (D.4) for $\hat{h}_e^{\text{estim}}$, the analytical estimate of the equilibrium front gap at the vertex is

$$\hat{h}_e^{\text{estim}} = \frac{1}{1+1/R_A}, \tag{D.5}$$

which approaches the value of the standard front gap $h_e^{\text{std}} = 1$ in the limit of large $|R_A|$, as expected from plane electrodes.

References

Alder, G., Clifton, D., Mill, F., 2000. A direct analytical solution to the tool design problem in electrochemical machining under steady state conditions. Proc. Inst. Mech. Eng. Part B: J. Eng. Manuf. 214 (8), 745–750.

Alkire, R., Bergh, T., Sani, R., 1978. Predicting electrode shape change with use of finite element methods. J. Electrochem. Soc. 125 (12), 1981–1988.

Bannard, J., 1977. Electrochemical machining. J. Appl. Electrochem. 7 (1), 1–29.

Białecki, R., Nahlik, R., Łapkowski, M., 1984. Applying the boundary element method to electrochemical calculations of primary current distribution. Electrochim. Acta 29 (7), 905–910.

Butt, R., 1993. Optimum design with finite-elements – design of electrochemical machining. J. Comput. Appl. Math. 47 (2), 151–165.

Céa, J., 1986. Conception optimale ou identification de formes, calcul rapide de la dérivée directionnelle de la fonction coût. Model. Math. Anal. Numer. 20, 371–402.

Chang, C., Hourng, L., 2001. Two-dimensional two-phase numerical model for tool design in electrochemical machining. J. Appl. Electrochem. 31 (2), 145–154.

Das, S., Mitra, A.K., 1992. Use of boundary element method for the determination of tool shape in electrochemical machining. Int. J. Numer. Methods Eng. 35 (5), 1045–1054.

Datta, M., 1993. Anodic dissolution of metals at high rates. IBM J. Res. Dev. 37 (2), 207–226.

Davydov, A.D., Volgin, V.M., Lyubimov, V.V., 2004. Electrochemical machining of metals: fundamentals of electrochemical shaping. Russ. J. Electrochem. 40 (12), 1230–1265.

De Barr, A., Oliver, D., 1968. Electrochemical Machining. MacDonald & Company, London.

Deconinck, D., Van Damme, S., Deconinck, J., 2012a. A temperature dependent multi-ion model for time accurate numerical simulation of the electrochemical machining process. Part II: numerical simulation. Electrochim. Acta 69, 120–127.

Deconinck, D., Van Damme, S., Deconinck, J., 2012b. A temperature dependent multi-ion model for time accurate numerical simulation of the electrochemical machining process. Part I: theoretical basis. Electrochim. Acta 60, 321–328.

Deconinck, J., 1994. Mathematical modelling of electrode growth. J. Appl. Electrochem. 24 (3), 212–218.

Elliott, C.M., 1980. On a variational inequality formulation of an electrochemical machining moving boundary-problem and its approximation by the finite-element method. J. Inst. Math. Appl. 25 (2), 121–131.

Eppler, K., Harbrecht, H., 2012. Shape optimization for free boundary problems – analysis and numerics. Int. Ser. Numer. Math. 160, 277–288.

Faust, C. (Ed.), 1971. Fundamentals of Electrochemical Machining. Electrodeposition Division and Electrothermics and Metallurgy Division, Electrochemical Society, Inc., Princeton, New Jersey.

Fitz-Gerald, J.M., McGeough, J.A., 1969. Mathematical theory of electrochemical machining: 2. anodic shaping. J. Inst. Math. Appl. 5, 409–421.

Fragalà, I., Gazzola, F., 2008. Partially overdetermined elliptic boundary value problems. J. Differ. Equ. 245 (5), 1299–1322.

Frank, M., Wolfe, P., 1956. An algorithm for quadratic programming. Naval Res. Logist. 3 (1–2), 95–110.

Fujisawa, T., Inaba, K., Yamamoto, M., Kato, D., 2008. Multiphysics simulation of electrochemical machining process for three-dimensional compressor blade. J. Fluids Eng. Trans. ASME 130 (8), 081602.

Gauger, N., Ilic, C., Schmidt, S., Schulz, V., 2012. Non-parametric aerodynamic shape optimization. In: Constrained Optimization and Optimal Control for Partial Differential Equations, International Series of Numerical Mathematics, vol. 160. Springer Basel, pp. 289–300.

Hardisty, H., Mileham, A.R., 1999. Finite element computer investigation of the electrochemical machining process for a parabolically shaped moving tool eroding an arbitrarily shaped workpiece. Proc. Inst. Mech. Eng. Part B: J. Eng. Manuf. 213 (8), 787–798.

Hourng, L., Chang, C., 1993. Numerical simulation of electrochemical drilling. J. Appl. Electrochem. 23 (4), 316–321.

Hunt, R., 1990. An embedding method for the numerical-solution of the cathode design problem in electrochemical machining. Int. J. Numer. Methods Eng. 29 (6), 1177–1192.

Ibl, N., 1981. Nomenclature for transport phenomena in electrolytic systems. Pure Appl. Chem. 53 (10), 1827–1840.

Jameson, A., Martinelli, L., 2000. Aerodynamic Shape Optimization Techniques Based on Control Theory. Springer, Berlin.

Jasak, H., Jemcov, A., Tuković, Z., 2007. OpenFOAM: A C++ library for complex physics simulations. In: International Workshop on Coupled Methods in Numerical Dynamics, pp. 47–66.

Jasak, H., Tuković, Z., 2006. Automatic mesh motion for the unstructured finite volume method. Trans. FAMENA 30 (2), 1–20.

Kiniger, B., Vexler, B., 2013. A priori error estimates for finite element discretizations of a shape optimization problem. ESAIM: Math. Modell. Numer. Anal. 47 (6), 1733–1763.

Kozak, J., 1998. Mathematical models for computer simulation of electrochemical machining processes. J. Mater. Process. Technol. 76, 170–175.

Krylov, A.L., 1968. The Cauchy problem for the Laplace equation in the theory of electrochemical metal machining. Sov. Phys. Doklady 13, 15–17.

Lacey, A.A., 1985. Design of a cathode for an electromachining process. Ima J. Appl. Math. 34 (3), 259–267.

Lamphere, M., Graham, J., Robertson, R., 2007. Tandem blisk electrochemical machining. US Patent 7,204,926.
Lions, J., 1968. Contrôle optimal de systèmes gouvernés par des équations aux dérivées partielles. Dunod-Gauthier-Villars, Paris.
Liu, W.B., Rubio, J.E., 1991. Optimal shape design for systems governed by variational-inequalities, Part 1: existence theory for the elliptic case. J. Optim. Theory Appl. 69 (2), 351–371.
Löhner, R., Yang, C., 1996. Improved ALE mesh velocities for moving bodies. Commun. Numer. Methods Eng. 12 (10), 599–608.
Mao, K.-W., 1971. ECM study in a closed-cell system. II. NaCl, $NaClO_4$, and $NaNO_3$. J. Electrochem. Soc. 118 (11), 1876–1879.
McClennan, J., Alder, G., Sherlock, A., Mill, F., Clifton, D., 2006. Two-dimensional tool design for two-dimensional equilibrium electrochemical machining die-sinking using a numerical method. Proc. Inst. Mech. Eng. Part B: J. Eng. Manuf. 220 (May (5)), 637–645.
McGeough, J.A., 1974. Principles of Electrochemical Machining. Chapman and Hall, London.
Murat, F., Simon, J., 1976. Sur le contrôle par un domaine géométrique. Technical Report, Laboratoire d'Analyse Numérique, Université Paris VI, Paris.
Narayanan, O.H., Hinduja, S., Nobel, C.F., 1986. Design of tools for electrochemical machining by the boundary element method. Proc. Inst. Mech. Eng. Part C J. Mech. Eng. Sci. 200 (3), 195–205.
Nilson, R., Tsuei, Y., 1974. Inverted Cauchy problem for the Laplace equation in engineering design. J. Eng. Math. 8 (4), 329–337.
Othmer, C., deVilliers, E., Weller, H.G., 2007. Implementation of a continuous adjoint for topology optimization of ducted flows. In: 18th AIAA Computational Fluid Dynamics Conference.
Patankar, S., 1980. Numerical Heat Transfer and Fluid Flow. McGraw-Hill, New York.
Pironneau, O., 1984. Optimal Shape Design for Elliptic Systems. Springer, New York.
Prentice, G.A., Tobias, C.W., 1982. A survey of numerical methods and solutions for current distribution problems. J. Electrochem. Soc. 129 (1), 72–78.
Purcar, M., Bortels, L., den Bossche, B.V., Deconinck, J., 2004. 3D electrochemical machining computer simulations. J. Mater. Process. Technol. 149 (1–3), 472–478 14th International Symposium on Electromachining (ISEM XIV).
Rajurkar, K., Zhu, D., McGeough, J., Kozak, J., De Silva, A., 1999. New developments in electro-chemical machining. CIRP Ann. Manuf. Technol. 48 (2), 567–579.
Reddy, M.S., Jain, V.K., Lal, G.K., 1988. Tool design for ECM: correction factor method. J. Eng. Ind. 110 (2), 111–118.
Sautebin, R., Froideveaux, H., Landolt, D., 1980. Theoretical and experimental modeling of surface leveling in ECM under primary current distribution conditions. J. Electrochem. Soc. 127 (5), 1096–1100.
Schmidt, S., Ilic, C., Schulz, V., Gauger, N.R., 2011. Airfoil design for compressible inviscid flow based on shape calculus. Optim. Eng. 12 (3), 349–369.
Schuster, R., Kirchner, V., Allongue, P., Ertl, G., 2000. Electrochemical micromachining. Science 289 (5476), 98–101.
Sokołowski, J., Zolésio, J., 1992. Introduction to Shape Optimization: Shape Sensitivity Analysis. Springer Series in Computational Mathematics. Springer, Berlin.
Sun, C., Zhu, D., Li, Z., Wang, L., 2006. Application of FEM to tool design for electrochemical machining freeform surface. Finite Elem. Anal. Des. 43 (2), 168–172.
Tipton, H., 1971. Calculation of tool shape for ECM. In: Faust, C.L. (Ed.), Fundamentals of Electrochemical Machining. Electrochemical Society Softbound Symposium Series, Princeton, pp. 87–102.
Zhou, Y., Derby, J.J., 1995. The cathode design problem in electrochemical machining. Chem. Eng. Sci. 50 (17), 2679–2689.
Zhu, D., Wang, K., Yang, J., 2003. Design of electrode profile in electrochemical manufacturing process. CIRP Ann. Manuf. Technol. 52 (1), 169–172.